Boundary-Structure-Aware Transfer Functions for Volume Classification

Lina Yu
University of Nebraska-Lincoln
Lincoln, Nebraska, USA
lina@cse.unl.edu

Hongfeng Yu
University of Nebraska-Lincoln
Lincoln, Nebraska, USA
yu@cse.unl.edu

ABSTRACT

We present novel transfer functions that advance the classification of volume data by combining the advantages of the existing boundary-based and structure-based methods. We introduce the usage of the *standard deviation of ambient occlusion* to quantify the variation of both boundary and structure information across voxels, and name our method as *boundary-structure-aware transfer functions*. Our method gives concrete guidelines to better reveal the interior and exterior structures of features, especially for occluded objects without perfect homogeneous intensities. Furthermore, our method separates these patterns from other materials that may contain similar average intensities, but with different intensity variations. The proposed method extends the expressiveness and the utility of volume rendering in extracting the continuously changed patterns and achieving more robust volume classifications.

CCS CONCEPTS

• **Human-centered computing** → **Scientific visualization**;

KEYWORDS

Transfer functions, volume rendering, classification.

ACM Reference Format:
Lina Yu and Hongfeng Yu. 2017. Boundary-Structure-Aware Transfer Functions for Volume Classification. In *Proceedings of SA '17 Symposium on Visualization*. ACM, New York, NY, USA, 8 pages.
https://doi.org/10.1145/3139295.3139306

1 INTRODUCTION

One of the critical components of direct volume rendering is the design of a transfer function to make the features of interest visible by mapping voxel values to opacities and colors. An effective transfer function can assist scientists in classifying different materials and exploring inherent spatial relationships of a volume data. Most research on the use of transfer functions has focused on the visualization of *boundaries* between materials [Kindlmann and Durkin 1998; Lum and Ma 2004] or the occluded materials with consistent *structures* [Correa and Ma 2008, 2011; Lum et al. 2006].

However, boundary-based and structure-based methods could not meet the needs where a scientist desires to add emphases to materials of interest without perfect boundaries or homogeneous structures, especially when other materials have similar average intensities to the areas of interest, but with different variations in intensities. For example, in a medical feet dataset shown in Figure 6 (a), vacuous bone marrow has an occlusion distribution clearly differentiated from skin, bone and vasculature, but may have the same intensity as muscles. In a combustion dataset, the holes generated from flames (shown in Figure 8 (a) and (b)) are not homogeneous and have almost the same intensities as ambient air. Using only the boundary-based or structure-based methods makes it hard to extract these areas, due to the spacial context and the similar or non-homogeneous intensity distributions.

In this paper, we present a novel visualization approach that combines the advantages of the boundary-based and structure-based methods. The major contributions of the paper are:

- We introduce the usage of the *standard deviation of ambient occlusion* on each direction to differentiate surrounding information, and thereby identify object *structures* in a more robust manner.
- We apply the *divergence* operation on the gradient to transform a continuously changed area into a region with consistent intensity, and thereby enhance the identification of *boundaries*.
- We introduce new 2D transfer functions using the intensity field, the divergence field, and the field of the standard deviation of ambient occlusion. These transfer functions provide an intuitive user interface that can facilitate users to robustly distinguish interior and exterior materials from each other, especially for those materials with an imperfect homogeneous intensity distribution that are difficult to be identified using existing methods.

2 RELATED WORK

There has been a great amount of research devoted to transfer function design that is an indispensable part of volume visualization. Most existing methods can be roughly categorized into boundary-based methods and structure-based methods.

Boundary-based methods exploit voxel intensities and gradient properties to guide transfer function designs [Fujishiro et al. 1999; Guo et al. 2011; Lan et al. 2017; Lindholm et al. 2010; Takahashi et al. 2004; Wang et al. 2011]. The classic examples include Kindlmann and Durkin's approach of semi-automatic generation of transfer functions using the first and second derivatives for visualizing boundaries between materials [Kindlmann and Durkin 1998]. Lum and Ma [Lum and Ma 2004] presented lighting transfer functions to manipulate surface lighting and shading parameters at arbitrary scalar value transitions for enhancing material boundaries of interest. However, these boundary-based methods are not effective for volumes with a high amount of noise. Although the use of high

SA '17 Symposium on Visualization, November 27-30, 2017, Bangkok, Thailand

ACM ISBN 978-1-4503-5411-0/17/11.
https://doi.org/10.1145/3139295.3139306

ordered smoothing gradient estimation masks (such as Sobel Filter [Lum and Ma 2004]) helps suppress this noise, it can possibly blur the appearance of fine features of interest. Boundary-based methods are popular in visualization systems because they mostly use *local* information, which makes them easy to implement.

In recent years, researchers have recognized the limitations of these boundary-based methods. Structure-based methods, which attempt to move towards gathering more *global* information, have been proposed. Correa and Ma [Correa and Ma 2008] described a size-based approach to distinguish features with similar or identical intensities by the relative sizes of their features. Later they proposed an occlusion spectrum method to classify structures by the ambient occlusion of voxels [Correa and Ma 2009]. Curvatures have also been used to distinguish different structures according to their shapes [Kindlmann et al. 2003]. However, these structure-based approaches are most effective when features can be clearly separated from the background. In addition, they often need prior knowledge of the features, such as sizes, and are time-consuming by multiple-pass computations to select the best parameters. However, in practice, it is hard to know the exact size of the feature of interest in advance. Therefore, in cases where intensity may vary smoothly across the entire domain, occlusion-based or size-based methods cannot extract the entire object of interest. Furthermore, an isotropic diffusion filter is often used in these methods. This implies the difficulty to identify a feature larger than the filter.

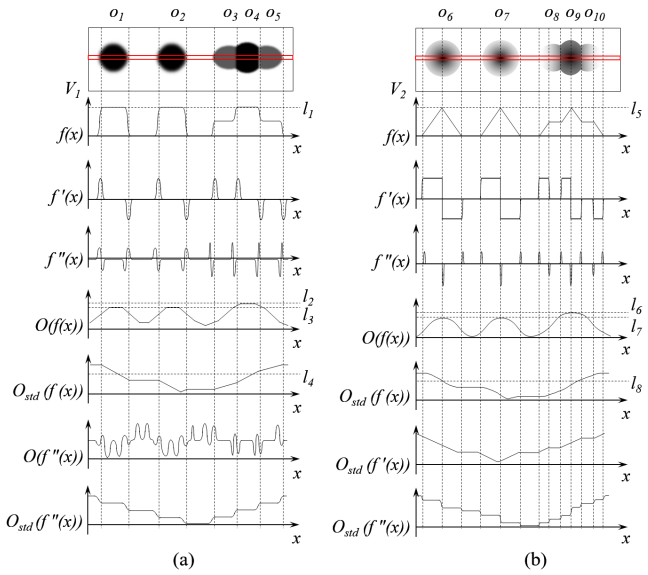

Figure 1: Comparison between the boundary-based method, the structure-based method, and our method for the objects with (a) homogeneous interiors and Gaussian boundaries and (b) continuously changed interiors.

3 BOUNDARY-STRUCTURE-AWARE TRANSFER FUNCTIONS

We aim to combine the advantages of boundary-based and structure-based approaches to volume classification. Specifically, our approach is based on the most seminal works presented by Kindlmann et al. [Kindlmann and Durkin 1998] and Correa et al. [Correa and Ma 2009]. We first revisit these two approaches to best present the rationale for our new transfer function design.

3.1 Boundary-Based Classification

Kindlmann et al. [Kindlmann and Durkin 1998] employed a Gaussian-based boundary model to compute the gradient of the intensity values for classifying a volume. For example, Figure 1 (a) shows a volume domain V_1 that consists of five objects o_1, o_2, o_3, o_4 and o_5, where o_1 and o_2 are surrounded by low intensities and o_4 is surrounded by o_3 and o_5 that have medium intensities. We assume that each object has a sharp, discontinuous change in its physical property and that it is blurred by a Gaussian at its boundary. The vertical dashed lines denote the boundary positions of these objects. Below the plot of V_1, we draw a 1D intensity profile $f(x)$ for the segment across the entire domain of V_1 (i.e., the red box in V_1). Then, we can compute and plot the first and second directional derivatives, $f'(x)$ and $f''(x)$, of $f(x)$. As Kindlmann et al. noted, an ideal location for the boundary would be defined by either the extremum in $f'(x)$ or the zero-crossing in $f''(x)$.

The combination of $f(x)$ and $f'(x)$ leads to 2D transfer functions that can effectively classify objects based on their boundaries and intensity values. However, this method only uses local information, and thus cannot further distinguish objects if they have the same intensity. For example, because o_1, o_2, and o_4 have the same intensity (denoted by the line l_1), we cannot distinguish them only using $f(x)$ and $f'(x)$. Similarly, we cannot separate o_3 and o_5 either.

3.2 Structure-Based Classification

To address this issue, researchers have proposed incorporating more structure information to enhance object classification. Correa et al. [Correa and Ma 2009] used the ambient occlusion of a voxel as a metric for classification. In computer graphics, ambient occlusion was proposed by Zhukov [Zhukov et al. 1998] using obscurance to model the ambient illumination of an object. It was used to improve the rendering of volumetric models, particularly for representing how each exposed point in a scene computes the ambient lighting on isosurfaces. The ambient occlusion of a point p can be computed by integrating the visibility function over the hemisphere Ω with respect to a projected solid angle:

$$AO(p) = \frac{1}{\pi} \oint_{\Omega} V_{p,\hat{\omega}}(\hat{n} \cdot \hat{\omega}) d\omega \tag{1}$$

where $V_{p,\hat{\omega}}$ is the visibility function at p along a direction $\hat{\omega}$, $\hat{n}$ represents the surface normal through p, and $d\omega$ is the infinitesimal solid angle step of the integration variable $\hat{\omega}$. This equation can be generalized to compute the occlusion of a voxel p in a volume as:

$$O(p, g) \approx \frac{1}{N} \sum_{\phi=0}^{\pi} \sum_{\theta=0}^{2\pi} A(p, \hat{\omega}(\theta, \phi), g) \tag{2}$$

where N is the number of neighbors of p, g is the input field (e.g., the scalar field $f(x)$). $A(p, \hat{\omega}, g)$ is the directional occlusion of p along direction $\hat{\omega}$ within the field g, defined as:

$$A(p, \hat{\omega}, g) = \sum_{t=0}^{T} M(p + t\hat{\omega}, g) \tag{3}$$

where T refers to the number of samples along the direction $\hat{\omega}$ and $M(p, g)$ is a visibility mapping function. $M(p, g)$ is application-specific. For example, for traditional isosurface applications, it can be a binary function that is 1 for the isovalue of interest, and is otherwise 0. Other functions, such as Gaussian weighted filters or linear ramps, are also commonly used. Equation 2 shows ambient occlusion can be considered as the convolution of the volume with a low pass filter where N is the size of the filter. It encodes the average contribution of the surrounding neighborhood and can help separate structures, as long as N is larger than the size of structures to be classified.

When this method is applied to the scalar field $f(x)$ in Figure 1 (a), the result is shown as the plot of $O(f(x))$. The occlusion values of $o_1(o_2)$ and o_4 are clearly different, which are indicated by the lines l_2 and l_3, respectively. This is because the surroundings of $o_1(o_2)$ and o_4 are different, as shown in V_1. This difference of occlusion allows us to easily separate these two objects, although they have the same intensity and cannot be separated using the boundary-based method. However, o_1 and o_2 have the same intensity and surrounding, resulting in the same occlusion indicated by l_3. In this case, we cannot separate them using occlusion. Moreover, we may not have prior knowledge of the size of objects before classification. In practice, this method often needs multiple-pass computations to find the best combination of parameters (i.e., M, T, N, etc.).

3.3 Rationale

Our goal is to design transfer functions that can distinguish objects with similar intensities, but different surroundings (e.g., o_2 and o_4 in Figure 1 (a)), as well as objects with similar intensities and surroundings, but different locations (e.g., o_1 and o_2 in Figure 1 (a)). Correa et al.'s method only considers the local information within the size of the filter. In this work, we advocate taking advantage of *global* information in the whole domain.

3.3.1 Standard Deviation of Ambient Occlusion. We notice that if we consider the information for the whole domain (i.e., use a filter that covers the whole domain), we still get the same occlusion for o_1 and o_2. This is because the occlusion value is equal to the summation of the values of M from all voxels, according to Equations 2 and 3. However, we observe that o_1 and o_2 have different variations within the directional occlusions (i.e., the results of the function A from Equation 3) along all directions. Hence, we express such a variation at a voxel p as the standard deviation of ambient occlusion:

$$O_{std}(p, g) = \sqrt{\frac{1}{H}\sum_{i=1}^{H}(A(p, \hat{\omega}_i, g))^2 - (\frac{1}{H}\sum_{i=1}^{H}A(p, \hat{\omega}_i, g))^2} \quad (4)$$

where H is the number of different directions.

We verify this idea by applying O_{std} on the scalar field $f(x)$ and plotting $O_{std}(f(x))$ in Figure 1 (a). For o_1 and o_2 that have the same $f(x)$ value, we can see that they can be clearly distinguished by the different values of the standard deviation of ambient occlusion based on $f(x)$, while they cannot be separated by only computing the summation of ambient occlusion $O(f(x))$ in Correa et al.'s method as discussed in Section 3.2. Intuitively, we can see that around o_1 and o_2 (e.g., the left and the right sides of each object in V_1) the global variation of ambient occlusion on $f(x)$ is different, which can be successfully quantified by Equation 4.

3.3.2 Field Transformation. It is effective to apply the standard deviation of ambient occlusion O_{std} on the scalar field $f(x)$ to tackle relatively simple cases (e.g., two objects o_1 and o_2). However, it has a few limitations when the data becomes more complex. When we add more objects (e.g., o_3, o_4, and o_5), some $O_{std}(f(x))$ values for an object may be the same as its surroundings or other objects. For example, in the $O_{std}(f(x))$ profile in Figure 1 (a), the line l_4 has the cross-sections with o_1 and o_4. Thus, we cannot accurately distinguish o_1 and o_4 according to their $O_{std}(f(x))$ values.

We observe that this issue is mainly caused by the non-zero intensity values of objects that are used as the input to the visibility mapping function M, but can reduce the influence of the surroundings. To address this issue, we incorporate the idea of the boundary-based methods, where we use $f'(x)$ or $f''(x)$ to transform the original scalar field into another field where only the boundary areas are highlighted and the other areas are suppressed, as shown as $f'(x)$ and $f''(x)$ in Figure 1 (a). If we use the occlusion function O to the field $f'(x)$ or $f''(x)$, we still cannot distinguish the objects, as shown by the example $O(f''(x))$ where o_1 and o_2 have similar values. Alternatively, if we use the standard deviation of ambient occlusion O_{std} to the field $f''(x)$, we can clearly classify all objects. As shown in $O_{std}(f''(x))$ in Figure 1 (a), each object corresponds to a unique value. We did not directly use $O_{std}(f'(x))$ in our approach because it is less appropriate in general cases, which will be detailed in Section 3.3.3.

We can extend $f''(x)$ to 3D scalar fields, which can be denoted by the divergence operation. The divergence of a vector field F, expressed as $div(F)$ or $\nabla \cdot F$, was originally defined by a limit of the surface integral:

$$\nabla \cdot F \equiv \lim_{V \to 0} \frac{\oint_s F \cdot ds}{V} \quad (5)$$

where the surface integral gives the value of F integrated over a closed infinitesimal boundary surface $S = \partial V$ surrounding a volume element V, which is taken to size zero using a limiting process. The divergence can also be denoted as the second derivative of the intensity $f(x, y, z)$:

$$\nabla^2 f(x, y, z) = \frac{\partial^2 f}{\partial x^2} + \frac{\partial^2 f}{\partial y^2} + \frac{\partial^2 f}{\partial z^2} \quad (6)$$

The divergence of the gradient of f is also commonly referred to as the Laplace operator or Laplacian, and results in a new scalar field $\nabla^2 f$. When the value of $\nabla^2 f$ in an area is 0, it implies that the change of the gradient is constant in this area, and thus this area is transformed to be homogeneous by the application of divergence. In this way, the originally continuously changed materials can be extracted with a constant divergence value, as the voxels in this part have constant changes in gradient values. Meanwhile, the boundaries can also be differentiated from possible noise or other less interesting features.

3.3.3 General Cases. In a more general case of imaging or scientific volume visualization, a scientist may need to add emphases to materials of interest that lack perfect homogeneous patterns, such as the feet and combustion datasets, shown in Figures 6 and 8. Kindlmann et al.'s boundary-based method can only extract the boundary of the structure by the 2D histogram of the intensity versus the second deviation, and it is hard to classify structures with similar

continuously changed intensities but at different locations, because the structures may have the same magnitudes of gradient vectors. Correa et al.'s structure-based method also encounters difficulty in accurately extracting these structures (e.g., the marrow from the foot MRI dataset, and the holes in the combustion dataset) due to the non-homogeneous interior intensities of these structures.

Compared to existing techniques, our novel approach extends the expressiveness and robustly classifies structures by bridging the advantage of boundary-based and structure-based methods, especially for extracting structures with imperfect homogeneous intensity distributions. Figure 1 (b) shows a volume domain V_2 that consists of five objects o_6, o_7, o_8, o_9 and o_{10}, where o_6 and o_7 are surrounded by low intensities and o_9 is surrounded by o_8 and o_{10} that have medium intensities. We assume that the each object has a continuous change in its physical property, as shown in the plot of $f(x)$ in Figure 1 (b), where the line l_5 indicates that o_6, o_7, and o_9 have the same maximum intensity.

In this case, $f'(x)$ is expressed as step functions, and the extrema cannot be considered as the indicators of the boundaries. Hence, Kindlmann et al.'s boundary-based method cannot be applied for classification using $f'(x)$. As shown in the plot of $O(f(x))$, Correa et al.'s structure-based method can distinguish the objects with the similar intensity but different surroundings, such as o_7 and o_9 that corresponds to the lines l_6 and l_7, respectively. However, it cannot distinguish objects with similar intensities and similar surroundings, such as o_6 and o_7.

Applying the standard deviation of ambient occlusion O_{std} on $f(x)$ can capture the global variation of surroundings of objects, and thereby allows us to classify o_6 and o_7, as shown in the plot of $O_{std}(f(x))$ in Figure 1 (b). However, when considering more objects, it also shows the same issue as its counterpart in Figure 1 (a), where the line l_8 has the cross-sections with o_6 and o_9. In this case, we first use $f''(x)$ to highlight the boundary areas and suppress the other areas, and then apply O_{std} on $f''(x)$. By combining the advantages of the boundary-based and structure-based methods, the resulting $O_{std}(f''(x))$ can perfectly separate each object with a unique value, as well as classify continuously changed areas.

Similar to $f(x)$ in Figure 1 (a), the step shapes of $f'(x)$ in Figure 1 (b) also reduces the influence of the surroundings in O_{std}. Thus, the shape of $O_{std}(f'(x))$ in Figure 1 (b) is similar to $O_{std}(f(x))$ in Figure 1 (a), and cannot be effectively used in this case. Given these cases, we did not use $O_{std}(f'(x))$ in our approach.

3.4 Transfer Function Design

We derive a new *boundary-structure-aware* transfer function design to address a general scalar field $f(x)$ that has relatively consistent or continuously changed intensities. The key of our boundary-structure-aware transfer functions is to use the standard deviation of ambient occlusion O_{std} (see Equation 4), which incorporates the global structure information of an input field g surrounding a voxel p and can have a different value for each object.

For a general volume data, we first use $f''(x)$ to highlight object boundaries and suppress object interiors, and thus transfer a potentially continuously changed region as a relatively constant region. Then, we use $f''(x)$ as the input field g, and compute the standard deviation of ambient occlusion $O_{std}(f''(x))$ of each ray

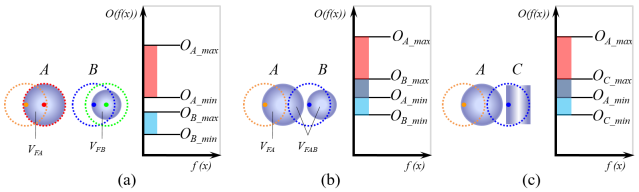

Figure 2: The properties of occlusion $O(f(x))$ with respect to object size (a), distance (b), and shape (c).

emitted from a voxel. In this way, we leverage the advantages of both the boundary-based and structure-based methods.

We establish a 2D classification space using the intensity values $f(x)$ or the second directional derivatives $f''(x)$ with the standard deviation of ambient occlusion $O_{std}(f''(x))$ from $f''(x)$. In our design, the horizontal dimension denotes $f(x)$ or $f''(x)$, while the vertical dimension corresponds to $O_{std}(f''(x))$. To change the opacity and the color of the selections, we use three additional 1D mappings with respect to $f(x)$, $f''(x)$, and $O_{std}(f''(x))$. When a structure is selected from the 2D histogram, the color and opacity values can be set individually according to $f(x)$, $f''(x)$, or $O_{std}(f''(x))$. This approach can simplify the complexity from high dimensional transfer functions, and a user can use multiple variables at one time to assign color and opacity values.

Therefore, we construct a boundary-structure-aware transfer function that is a mapping from the space spanned by $f(x)$ or $f''(x)$ and $O_{std}(f''(x))$ into color and opacity:

$$f(x) \times O_{std}(f''(x)) \mapsto [0, 1] \text{ or } f''(x) \times O_{std}(f''(x)) \mapsto [0, 1]. \quad (7)$$

By tagging different regions of the resulting 2D histogram and assigning color and opacity, users can select regions with similar continuously changed intensity values but in different locations within the dataset.

We note that in some special cases (e.g., a simple volume only consisting of two objects), the usage of $f(x)$ as the input field g works better than $f''(x)$. The reason is that after the computation of $f''(x)$, we only obtain the values of boundaries and other parts will be close to zero values in these cases. Thus, if there are two objects with the same intensities and sizes in the volume, they will have a very similar standard deviation of ambient occlusion based on $f''(x)$. In this case, we can use the method of computing the standard deviation of ambient occlusion based on $f(x)$. For example, as discussed in Section 3.3, o_1 and o_2 in V_1, and o_6 and o_7 in V_2 can be easily distinguished by $O_{std}(f(x))$. However, when more objects are involved in the volume, we recommend the method of computing the standard deviation of ambient occlusion based on $f''(x)$, because the $f''(x)$ operation helps us simplify the volume and it is also ready for the differentiation of the interior and exterior.

3.5 Properties

Our boundary-structure-aware transfer functions feature a set of proprieties that lead to robust classification with respect to various object changes in *size*, *distance*, *shape*, and *intensity*.

For comparison, we first use a simple example to illustrate the strengths and the possible limitations of Correa et al.'s method with respect to object size, distance, and shape. As shown in Figure 2

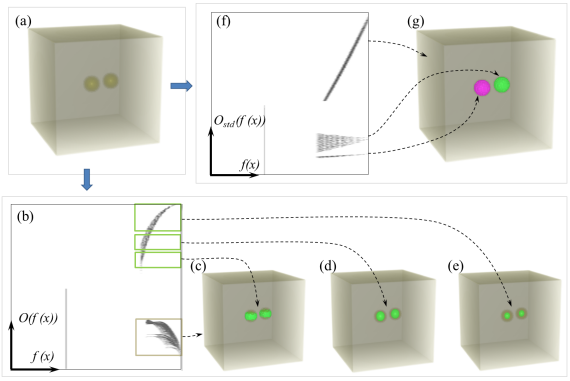

Figure 3: Comparison between Correa et al.'s method and our method to separate structures even though they share the same intensity, shape, size, and environment. The distance between two balls is less than the ball size.

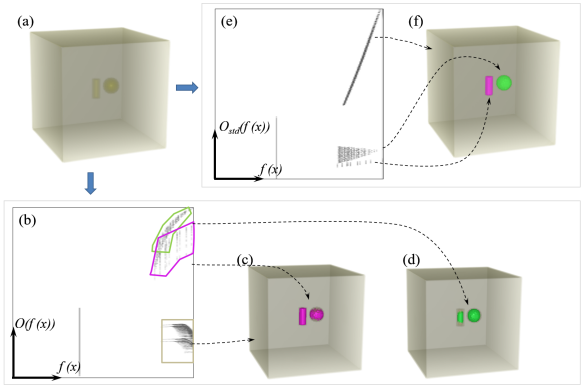

Figure 4: Comparison between Correa et al.'s method and our method to separate structures with the same intensity but different shapes. The distance between the two objects is smaller than the object sizes.

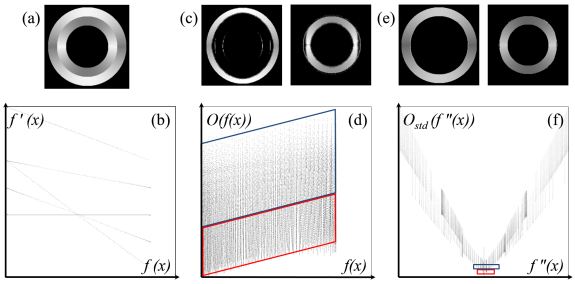

Figure 5: Comparison between Kindlmann et al.'s method (b), Correa et al.'s method ((c)-(d)), and our method ((e)-(f)) to separate structures using one synthetic dataset containing two nested cylinders with varying intensities ((a)).

(a), we assume that there are two 3D balls A and B with different sizes. We employ a filter F to compute the occlusion $O(f(x))$ for A and B using Equation 2. The filter is represented by a dotted circle in Figure 2 and has the size of the bigger ball A. We denote the volumes of A, B, and the filer F as V_A, V_B, and V_F, respectively, where $V_A = V_F > V_B$. Without loss of generality, we assume that A and B have the same intensity value of 1, and the intensity of the surroundings is 0. We also assume that, for any voxel, the value of the M function in Equation 3 is equal to its intensity value. Thus, the occlusion around a voxel p is the intersection volume of A and B with F, when F's center is at p.

We first let the distance between A and B be large enough in that the filter F cannot simultaneously intersect with both A and B, as shown in Figure 2 (a). We can easily see that the maximum occlusion O_{A_max} of A is V_A, when F and A are concentric (see the red point). When the center of F is at a boundary voxel of A (see the orange point), we gain the minimum occlusion O_{A_min} of A, which is the intersection volume V_{FA} of F and A. Similarly, the maximum occlusion O_{B_max} of B is V_B, when F and B are concentric (see the green point). When the center of F is at a boundary voxel of B (see the blue point), we obtain the minimum occlusion O_{B_min} of B, which is the intersection volume V_{FB} of F and B. Therefore, if $O_{B\_max} < O_{A\_min}$ (i.e., $V_B < V_{FA}$), Correa et al.'s method can perfectly distinguish A and B using the occlusion function $O(f(x))$, even though A and B have the same intensity value of $f(x)$, as shown in the 2D histogram in Figure 2 (a).

However, the condition of $O_{B\_max} < O_{A\_min}$ may not always hold with changes in object size, distance, or shape. For example, we can enlarge B in Figure 2 (a) to make $V_B > V_{FA}$, and thus gain $O_{B\_max} > O_{A\_min}$. Alternatively, we can keep the sizes of A and B unchanged but shorten the distance between them, as shown in Figure 2 (b). In this case, the filter F can possibly intersect with both A and B, when the center of F is at a boundary voxel of B (e.g., the blue point). The occlusion at the blue point is equal to the intersection volume V_{FAB} of F, A and B, and can be greater than V_{FA} at the orange point. Therefore, $O_{B\_max} > O_{A\_min}$ is gained. Similarly, the overlapping of the occlusion values can also happen in the case of two objects with a similar size but different shapes, as shown in Figure 2 (c). In these situations, the occlusion spectrum cannot perfectly distinguish objects.

Our method, which computes the standard deviation of ambient occlusion O_{std}, not only inherits the strengths of the occlusion spectrum, but also addresses its limitations. In this case that only consists of two objects, according to our discussion in Section 3.4, we choose $f(x)$ as the input field to show the effectiveness of the standard deviation of ambient occlusion O_{std} in classification.

3.5.1 Size and Distance. Similar to Correa et al.'s method, our method can classify objects with different sizes and at a sufficient distance. More importantly, our method can also classify nearby objects with the same size. For example, we create a synthetic 3D dataset where two balls are contained in a box, as shown in Figure 3 (a). The balls share the same intensity, shape, size, and environment. The balls and the box have the same intensity. The distance between two balls is less than the ball size. As shown in Figure 3 (b), the occlusion values of $O(f(x))$ of two balls overlap in the 2D histogram, where a single selected region (i.e., a green box) can be mapped to the partial structures on both balls, as shown in Figure 3 (c)-(e). This issue corresponds to the situation illustrated in Figure 2 (b). However, our method uses the $O_{std}(f(x))$ to encode the global structure information, and can help easily separate two balls. When we plot the intervals of $O_{std}(f(x))$ in a 2D histogram

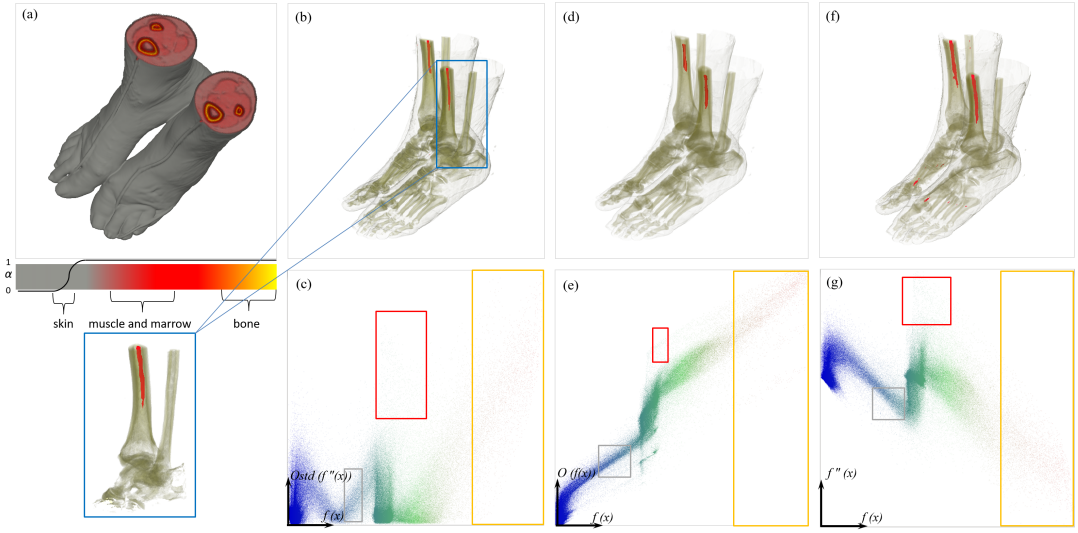

Figure 6: The classification of the marrow, bone and skin from the feet data using our method ((b)-(c)), Correa et al.'s method ((d)-(e)), and Kindlmann et al.'s method ((f)-(g)). In (c), (e), and (g), the opacity values are 1.0, 0.4 and 0.25 for the regions selected by the red, yellow and grey boxes, respectively.

(see Figure 3 (f)), we can obtain a clear separation of structures, and each of them is mapped to an individual ball (see Figure 3 (g)).

3.5.2 Shape. Our method can also classify nearby objects with different shapes. As shown in Figure 4 (a), the distance between the ball and the cylinder is smaller than their sizes. In this case, the occlusion values $O(f(x))$ of the two structures can partially overlap, leading to the difficulty in separation, as shown in Figure 4 (b)-(d). This issue corresponds to the situation illustrated in Figure 2 (c). Alternatively, our method uses $O_{std}(f(x))$ to capture the distinct variation of the neighborhood intensities of the objects, and thereby is more robust in classification, as shown in Figure 4 (e) and (f).

3.5.3 Intensity. As discussed in Section 3.3.3, apart from classifying objects with constant or relatively constant intensities, one unique property of our method is to tackle objects with varying intensities that are difficult to classify using the exiting boundary- and structure-based methods. Figure 5 (a) shows an example that contains two concentric nested cylinders in 3D. The inner cylinder has the intensity linearly changing from 1 to 0 to 1 to 0 along its circumference, while the intensity of the outer cylinder linearly changes from 0 to 1 to 0 to 1. The other areas have the same values of intensity 2. Figure 5 (b) shows a 2D histogram with the intensity $f(x)$ versus its first derivative $f'(x)$ using Kindlmann et al.'s method [Kindlmann and Durkin 1998]. Because this synthetic dataset does not follow the Gaussian-based boundary model, it is difficult to classify these two cylinders using this 2D histogram.

Figure 5 (c) shows the result using Correa et al.'s method [Correa and Ma 2009]. By selecting different regions in the 2D histogram with the intensity $f(x)$ versus the occlusion $O(f(x))$ in Figure 5 (d), it can mostly classify these two cylinders. However, the similar occlusion values can be generated within the two cylinders along the boundaries, and thus we cannot perfectly classify these areas.

Figure 5 (e) shows the result using our method. With the 2D histogram of the second derivatives $f''(x)$ and the standard deviation of ambient occlusion $O_{std}(f''(x))$ in Figure 5 (f), we can successfully distinguish the outer and inner cylinders. By computing the divergence of the gradient of $f(x)$, we can suppress the continuously changed intensity of each cylinder into a low constant value, and highlight the boundaries between these two cylinders. Then, we compute the standard deviation of ambient occlusion on the resulting $f''(x)$ field, and generate different values of the cylinders that exhibit the completely different surroundings using the global structure information. Therefore, we can see that each cylinder has a $f''(x)$ value close to zero (i.e., the middle point of the $f''(x)$ profile in Figure 5 (f)), but they have different $O_{std}(f''(x))$ values. We can clearly classify the outer and inner cylinders corresponding to the blue and red regions in the 2D histogram.

4 CASE STUDIES

4.1 Imaging Datasets

Imaging is one of the most important tools to display 3D objects, and is widely used in various medical and engineering applications (e.g., evaluating size and form of tissue structures, and detecting defects in mechanical components). Example imaging methods include ultrasound, MRI, and CT [Karatas and Toy 2014]. An imaging data often has specific objects that can be expressed by the Gaussian-based boundary model (see Figure 1 (a), Sections 3.1 and 3.2).

We first apply our boundary-structure-aware transfer functions to an MRI scan of feet. Similar to the existing methods, our method can successfully classify the main structures such as bone, skin and muscle. More importantly, our method can also separate fine features, such as the marrow, from other tissues, which is hard to realize using the existing methods. As shown in Figure 6 (a), we can tell from the 1D transfer function that the marrow has the same intensity as the muscles between the bone and skin. The intensity values in the marrow are continuously changed, so it is hard to extract the marrow part only by those values. Figure 6 (d) and (e)

show the results using Correa et al.'s method and the corresponding transfer function with $O(f(x))$ and $f(x)$, respectively. We can see that the marrow part can only partially be extracted, if we want to extract all marrow part, other sectional areas with the same values of $O(f(x))$ and $f(x)$ will also be detected. Figure 6 (f) and (g) show the results using Kindlmann et al.'s method and the corresponding transfer function with $f''(x)$ and $f(x)$, respectively. In this example, a part of instep areas has the same $f''(x)$ and $f(x)$) values as the marrow. Thus, the marrow part cannot be accurately separated by the structure-based method and the boundary-based method. This verifies our rationale shown in Figure 1 that Correa et al.'s and Kindlmann et al.'s methods hardly distinguish objects at different locations with similar intensities and similar surroundings.

Our method works well on this kind of datasets. Here, we use the intensity versus the standard deviation of ambient occlusion based on the divergence (i.e., $f(x)$ versus $O_{std}(f''(x))$) as a 2D classification space. The reason why we choose the intensity $f(x)$ as one of the metrics is that we can easily identify the bone and skin by the different intensity values. Thus, it is easy for us to roughly identify each part in a classification space. The occlusion axis helps us separate the objects with similar intensities, but different locations. We assign the color to each point on the histogram based on the divergence $f''(x)$ to help a user better distinguish the boundary. Because the divergence $f''(x)$ helps us transfer the continuously changed region to a relatively constant intensity, computing the standard deviation of ambient occlusion based on the divergence assists us in finding the occluded marrow in fociles and separate it from muscles and the marrow in toes. Figure 6 (b) shows our classification results for the feet data, while the image (c) shows a 2D classification space based on $f(x)$ versus $O_{std}(f''(x))$. It can be seen that the marrow, shown in red in the image (b), can be extracted by brushing the red region in the image (c). The yellow and gray regions in the image (c) correspond to bone and skin, respectively. This marrow structure cannot be accurately extracted by the existing boundary-based and structure-based methods.

We also apply our boundary-structure-aware transfer function to a CT scan of engine data. Our method can not only depict the main structure of the engine, but also extract the fine features, such as the stick-shape holes, and separate the holes at different locations respectively. Figure 7 (a) and (b) are the results from Kindlmann et al.'s method. We can see that this method extracts the holes simultaneously and cannot independently display either one because two stick-shape holes share the same $f(x)$ and $f''(x)$ values, and another circular hole with the same $f(x)$ and $f''(x)$ is also extracted. However, our method (shown in (c)) separates the two holes by a 2D classification space that consists of the divergence of intensity versus the standard deviation of ambient occlusion based on the divergence (i.e., $f''(x)$ versus $O_{std}(f''(x))$) as shown in the image (d). When we use Correa et al.'s method to extract the hole in the middle, the boundary of engine structure and partial hole nearby will also be extracted as shown in the image (e).

4.2 Scientific Simulation Datasets

Visualizing scientific simulation datasets is another important application. Different from imaging datasets, scientific simulation datasets are often characterized with continuously changed scale

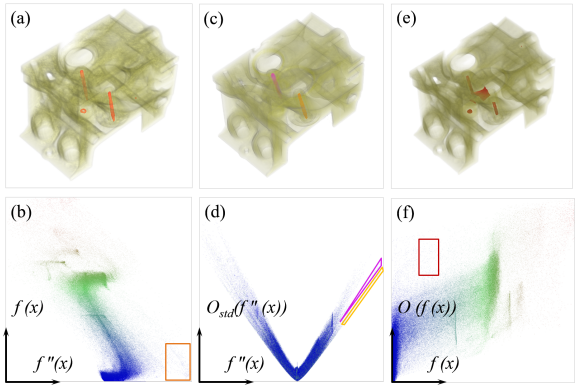

Figure 7: The classification of the holes in the engine data using Kindlmann et al.'s method ((a)-(b)), our method ((c)-(d)), and Correa et al.'s method ((e)-(f)). The opacity values are 1.0, 1.0 and 0.4 for the regions selected by the red, orange and yellow boxes, respectively.

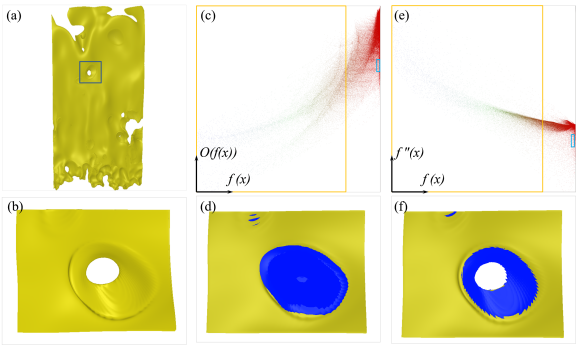

Figure 8: (a) shows a side view of a combustion data. (b) shows a hole and its boundary on a slab in the selected region of (a), which are classified using Correa et al.'s method ((c)-(d)) and Kindlmann et al.'s method ((e)-(f)).

fields, where generally 3D features cannot be expressed by the Gaussian-based boundary model (see Figure 1 (b) and Section 3.3.3).

Figure 8 (a) shows an example dataset generated from a combustion simulation, which contains an isosurface of a flame structure. The scientists are interested in extracting the holes on the surface. Figure 8 (b) shows a hole on an extracted slab. These holes correspond to a sudden drop in the intensity values, corresponding to the extinction event. The classification of the holes in the combustion simulation helps the scientists analyze the extinguished areas and investigate the underlying chemical and physical processes, which is critical to improving combustion efficiency.

However, the intensities of the holes in the combustion dataset are most continuously changed and have similar intensities as air. This hole structure cannot be identified only using the gradient or the occlusion information with the traditional methods. By comparison, Correa et al.'s method shown in Figure 8 (c)-(d) cannot exactly extract the holes while Kindlmann et al.'s method shown in Figure 8 (e)-(f) can only extract hole's boundary. In addition, a portion of the upper-left region (in blue) is also misclassified with the central hole using these two methods.

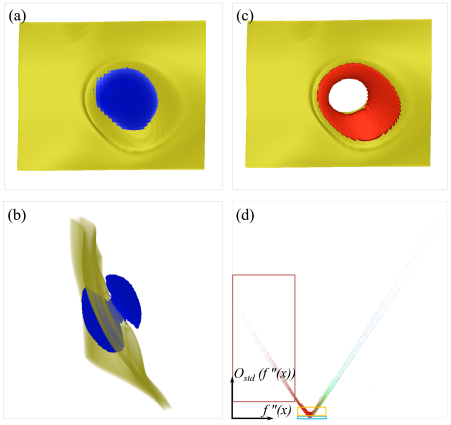

Figure 9: The classification of the hole and its boundary in the combustion data using our method. The opacity values are 1.0, 1.0 and 0.5 for the regions selected by the red, blue, and yellow boxes.

We apply our method using the divergence $f''(x)$ versus the standard deviation of the occlusion based on the divergence $O_{std}(f''(x))$ as a 2D classification space as shown in Figure 9 (d). The reason is that we can easily identify the area in the space with zero divergence and lowest standard deviation of ambient occlusion, as the hole occluded in the volume and the region with higher occlusions and lowest negative and highest positive divergences correspond to the boundary. Figure 9 shows classification results from applying our method to the combustion dataset. We can easily extract the hole shown as the blue color in the image (a), corresponding to the area in the blue box in the image (d). The image (b) shows the side view of this hole of which intensities are continuously changed. The red area in the image (d) denotes the lower divergence, which is the boundary of the hole colored by red in Figure 9 (c). The area in the yellow box in the image (d) corresponds to the flame colored by yellow in the images (a), (b) and (c).

We also apply our method to another combustion simulation case in Figure 10. Our boundary-structure-aware transfer function can identify the specially shaped hole, shown as the red color in the image (a), on the frame structure shown in the image (b). The image (c) shows the corresponding 2D histogram based on $f(x)$ versus $O_{std}(f''(x))$, and the corresponding selected region in the light red box. The images (d)-(f) show the cutaway from the side view of our method ((d)) and 1D transfer function based on intensity without air ((e)) and with air ((f)). The image (f) clearly shows that the hole and the air have the similar intensity, and are hard to be separated using the traditional methods.

5 CONCLUSION

This paper presents boundary-structure-aware transfer functions for volume classification. We introduce a novel method to make use of the standard deviation of ambient occlusion to enhance classifying 3D volume datasets. In addition, we apply divergence along the gradient as one of the main criteria for classification. Our method can not only highlight the boundaries, but also accurately distinguish objects that may be occluded or have continuously changed patterns. Our work shows a promising approach to help scientists explore their data with more detailed and robust classifications.

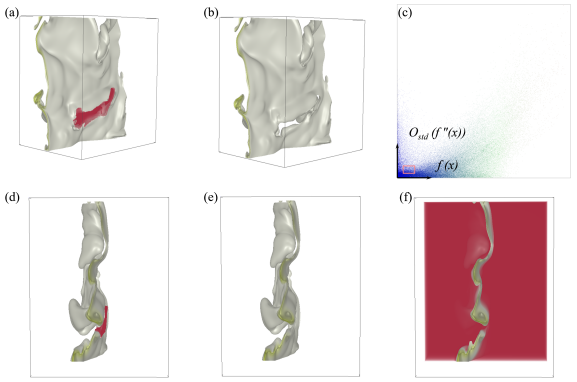

Figure 10: The classification of the hole in another combustion data using our method.

ACKNOWLEDGMENTS

This research has been sponsored by the National Science Foundation through grants IIS-1423487 and ICER-1541043. The combustion datasets were provided by Dr. Jacqueline H. Chen at Sandia National Laboratories.

REFERENCES

Carlos Correa and Kwan-Liu Ma. 2008. Size-based transfer functions: A new volume exploration technique. *Visualization and Computer Graphics, IEEE Transactions on* 14, 6 (2008), 1380–1387.

Carlos Correa and Kwan-Liu Ma. 2009. The occlusion spectrum for volume classification and visualization. *Visualization and Computer Graphics, IEEE Transactions on* 15, 6 (2009), 1465–1472.

Carlos Correa and Kwan-Liu Ma. 2011. Visibility histograms and visibility-driven transfer functions. *Visualization and Computer Graphics, IEEE Transactions on* 17, 2 (2011), 192–204.

Issei Fujishiro, Taeko Azuma, and Yuriko Takeshima. 1999. Automating transfer function design for comprehensible volume rendering based on 3D field topology analysis. In *Visualization'99. Proceedings.* IEEE, 467–563.

Hanqi Guo, He Xiao, and Xiaoru Yuan. 2011. Multi-dimensional transfer function design based on flexible dimension projection embedded in parallel coordinates. In *Visualization Symposium (PacificVis), 2011 IEEE Pacific.* IEEE, 19–26.

Orhan Hakki Karatas and Ebubekir Toy. 2014. Three-dimensional imaging techniques: A literature review. *European journal of dentistry* 8, 1 (2014), 132.

Gordon Kindlmann and James W Durkin. 1998. Semi-automatic generation of transfer functions for direct volume rendering. In *Proceedings of the 1998 IEEE symposium on Volume visualization.* ACM, 79–86.

Gordon Kindlmann, Ross Whitaker, Tolga Tasdizen, and Torsten Moller. 2003. Curvature-based transfer functions for direct volume rendering: Methods and applications. In *Visualization, 2003. VIS 2003. IEEE.* IEEE, 513–520.

Shouren Lan, Lisheng Wang, Yipeng Song, Yu-ping Wang, Liping Yao, Kun Sun, Bin Xia, and Zongben Xu. 2017. Improving Separability of Structures with Similar Attributes in 2D Transfer Function Design. *Visualization and Computer Graphics, IEEE Transactions on* 23, 5 (2017), 1546–1560.

Stefan Lindholm, Patric Ljung, Claes Lundström, Anders Persson, and Anders Ynnerman. 2010. Spatial conditioning of transfer functions using local material distributions. *Visualization and Computer Graphics, IEEE Transactions on* 16, 6 (2010), 1301–1310.

Eric B Lum and Kwan-Liu Ma. 2004. Lighting transfer functions using gradient aligned sampling. In *Proceedings of the conference on Visualization'04.* IEEE Computer Society, 289–296.

Eric B Lum, James Shearer, and Kwan-Liu Ma. 2006. Interactive multi-scale exploration for volume classification. *The Visual Computer* 22, 9-11 (2006), 622–630.

Shigeo Takahashi, Yuriko Takeshima, and Issei Fujishiro. 2004. Topological volume skeletonization and its application to transfer function design. *Graphical Models* 66, 1 (2004), 24–49.

Yunhai Wang, Jian Zhang, Wei Chen, Huai Zhang, and Xuebin Chi. 2011. Efficient opacity specification based on feature visibilities in direct volume rendering. *Computer Graphics Forum* 30, 7 (2011), 2117–2126.

Sergey Zhukov, Andrei Iones, and Grigorij Kronin. 1998. An ambient light illumination model. In *Rendering Techniques '98.* Springer, 45–55.